Available online at www.sciencedirect.com
SCIENCE DIRECT®
Comput. Methods Appl. Mech. Engrg. 194 (2005) 775–800
Computer methods in applied mechanics and engineering
www.elsevier.com/locate/cma

Stabilized finite element formulation for elastic–plastic finite deformations

Binoj Ramesh, Antoinette M. Maniatty *

Department of Mechanical, Aerospace, and Nuclear Engineering, Rensselaer Polytechnic Institute, 110 8th Street, Troy, NY 12180, USA

Received 8 November 2002; received in revised form 17 February 2004; accepted 7 June 2004

Abstract

This paper presents a stabilized finite element formulation for nearly incompressible finite deformations in hyperelastic–plastic solids, such as metals. An updated Lagrangian finite element formulation is developed where mesh dependent terms are added to enhance the stability of the mixed finite element formulation. This formulation circumvents the restriction on the displacement and pressure fields due to the Babuška–Brezzi condition and provides freedom in choosing interpolation functions in the incompressible or nearly incompressible limit, typical in metal forming applications. Moreover, it facilitates the use of low order simplex elements (i.e. P1/P1), reducing the degrees of freedom required for the solution in the incompressible limit when stable elements are necessary. Linearization of the weak form is derived for implementation into a finite element code. Numerical experiments with P1/P1 elements show that the method is effective in incompressible conditions and can be advantageous in metal forming analysis.

Keywords: Stabilized finite element method; Babuška–Brezzi condition; Hyperelasticity; Plasticity; Viscoplasticity

1. Introduction

Over the past three decades, considerable progress has been made in the the development of finite element formulations capable of modeling large elastic–plastic deformations, and today, FEM codes that have grown up from these developments are frequently used in industrial practice. Early formulations used objective, spatial, rate forms for defining the elastic part of the deformation, which resulted in convenient algorithms for updating the stress, see for example Hibbitt et al. [8], Needleman [22], and McMeeking and

* Corresponding author. Tel.: +1 518 276 6984; fax: +1 518 276 6025.
E-mail address: maniaa@rpi.edu (A.M. Maniatty).

0045-7825/$ - see front matter
doi:10.1016/j.cma.2004.06.025

Rice [20]. Such formulations are still commonly used today. The primary disadvantages of elastic rate formulations are that they, in most cases, allow elastic dissipation and require small time steps to maintain accuracy. An exception to this is the formulation proposed by Xiao et al. [34], which is based on a rate of the Eulerian logarithmic strain measure and does not exhibit dissipation. Simo and co-workers [26–29] developed a general formulation that uses a hyperelastic constitutive equation to avoid the problem of elastic dissipation and allow for larger time steps leading to more efficient algorithms. Weber and Anand [32] and Eterovic and Bathe [6] present formulations that use a hyperelastic constitutive model based on the Lagrangian, logarithmic strain measure assuming isotropic and combined isotropic-kinematic hardening, respectively. In those works and many others (for example, Moran et al. [23] and Miehe et al. [21]), a multiplicative decomposition of the deformation gradient into elastic and plastic parts, as proposed by Lee [15], is also assumed. The use of the Lagrangian, logarithmic strain measure together with the multiplicative decomposition of the deformation gradient has several advantages, both in the formulation of constitutive models and in the associated computational formulation. To be specific, the resulting return mapping algorithm is similar to that of small deformation elasto-plasticity. Furthermore, it results in an additive decomposition of the elastic and plastic strains in the absence of rotations, and the Lagrangian logarithmic strain, for isotropically elastic materials, has a simple work conjugate stress measure, as shown by Hogar [10]. However, the latter advantage and usefulness of the Lagrangian logarithmic strain measure is lost if the elastic behavior of the material is not isotropic.

An important consideration in modeling large deformation elastic–plastic processes by the finite element method is the nearly incompressible behavior, typical in metals. To handle the near incompressibility, a mixed formulation is used where the displacement and pressure fields are interpolated separately [2]. Due to plastic incompressibility, severe mesh locking and unphysical pressure oscillations may occur unless the finite element interpolation functions satisfy the Babuška–Brezzi or inf–sup condition [1]. The Babuška–Brezzi theory imposes certain conditions on the interpolation functions in order to guarantee unique solvability and convergence. Hence the solution spaces for displacement and pressure cannot be chosen independently when the discretization is based on the Galerkin method. This problem has been studied thoroughly and several displacement–pressure combinations that satisfy the Babuška–Brezzi condition are known. Unfortunately, many lower order elements, including the P1/P1 element with linear interpolation for displacement and pressure, do not satisfy this condition and exhibit severe mesh locking. Hence, attention is focussed in this work to stabilize the low order P1/P1 elements.

Stabilized finite element methods consist of adding mesh dependent terms, which are functions of the residuals of the Euler–Lagrange equations evaluated element-wise, to the standard Galerkin method [11,12,14,17]. With the addition of the stabilization terms, the consistency is not sacrificed since the exact solution satisfies both the stabilization and Galerkin terms. Using this stabilization technique, it is possible to avoid the stability problems that are seen with classical mixed methods when the interpolation does not satisfy the Babuška–Brezzi condition. This permits freedom in choosing interpolations for the displacement and pressure field, including equal order interpolations, and as a result, are well suited for p-adaptivity.

Stabilized finite elements have been used in fluid mechanics for incompressible flows and convection dominated flows, as well as for related problems in linear elasticity. They were first introduced by Hughes et al. [11] for incompressible stokes flow, the equations of which are similar to that of incompressible linear elasticity. That early formulation was limited to continuous pressure elements. Later, Hughes and Franca [12] extended the formulation for the stokes problem to one that converges for all velocity/pressure spaces, including discontinuous pressure fields, by adding stabilization terms consisting of jumps in pressures across element interfaces. One of the advantages of this formulation is that it results in symmetric matrices. However, these pressure jump terms need a non-standard assembly procedure and the nodal pressure cannot be eliminated at the element level due to the coupling introduced by these jump terms, thus eliminating the primary advantage of discontinuous pressure elements. Franca et al. [7] show that under certain assumptions these additional jump terms are unnecessary. These assumptions, however, preclude the use

of linear stabilized elements without the pressure jump stabilization terms. Hughes et al. [11,12] derive error estimates for the convergence of their stabilized elements for the stokes problem and linear elasticity. In Hughes [13], a relationship is established between subgrid scale models and stabilized methods. Based on this concept, Chiumenti et al. [5] proposed a stabilized formulation for small elastic strain analysis using orthogonal subgrid scales.

Recently, the stabilized finite element method has been extended to problems involving finite deformations in solids. Klaas et al. [14] adapted the formulation presented in Hughes et al. [11] for large deformation hyperelasticity with linear P1/P1 elements. This formulation was later extended to higher order interpolation functions by Maniatty et al. [18] using a local reconstruction method to construct part of the stabilization terms. Maniatty et al. [17,19] also present a formulation for steady state flow problems to analyze forming processes such as drawing. In that formulation, a mixed velocity/pressure formulation was used, similar to that used in problems involving flowing fluids. In this paper, the method is extended to non-steady, finite elasto-plasticity using a mixed displacement/pressure field formulation.

The form of the governing kinematic and constitutive equations used herein follow that considered in Weber and Anand [32] and Eterovic and Bathe [6]. Specifically, a multiplicative decomposition of the deformation gradient into elastic and plastic part is assumed [15], with the plastic part being isochoric. Both rate independent and rate dependent, isotropic constitutive laws are considered.

The intention of this paper is to extend the use of stabilized finite element methods to finite deformation elasto-plasticity, where the use of stable elements are required due to plastic incompressibility. We concentrate on P1/P1 elements and continuous interpolation of pressure as discontinuous pressure elements are not advantageous in the stabilization of linear elements because of the need for jump terms as described earlier.

The outline of the paper is as follows. In the next section, we list the basic governing equations for isotropic, finite deformation elasto-plasticity. Section 3 summarizes the integration procedure used to integrate the constitutive equations. In Section 4, the proposed stabilized Petrov–Galerkin formulation, to circumvent the Babuška–Brezzi condition in nearly incompressible situations arising from large plastic deformations, is introduced. The consistent linearization required for quadratic convergence is presented in Section 5 for implementation into a finite element code. Finally, four numerical examples are presented to test the behavior of stabilized finite elements under plastic incompressibility and conclusions are drawn.

2. Governing equations

For completeness, the basic governing equations for isotropic, finite deformation elasto-plasticity are given. Consider the motion of the body occupying configuration B_0 at time $t = 0$ under the action of external forces. The position of the body at a time t is given by

$$\boldsymbol{x} = \boldsymbol{\varphi}(\boldsymbol{X}, t), \tag{1}$$

where $\boldsymbol{X}$ is a point on the initial reference configuration B_0 and $\boldsymbol{x}$ is the same material point in the deformed configuration B at time t. The deformation gradient is then $\boldsymbol{F} = \nabla\boldsymbol{\varphi}(\boldsymbol{X}, t)$. For the case of an updated Lagrangian analysis the reference configuration is updated at the end of each time step. The reference configuration at time $t = t_n$ will be B_n, and B_{n+1} is the current configuration at $t = t_{n+1}$. The relative deformation gradient is then

$$\boldsymbol{F}_r = \boldsymbol{F}_{n+1}\boldsymbol{F}_n^{-1}, \tag{2}$$

where $\boldsymbol{F}_n$ and $\boldsymbol{F}_{n+1}$ are the total deformation gradients at time $t = t_n$ and $t = t_{n+1}$, respectively.

For any given time, a multiplicative decomposition [15] of the deformation gradient into elastic and plastic components is assumed giving

$$\boldsymbol{F} = \boldsymbol{F}^{\mathrm{e}}\boldsymbol{F}^{\mathrm{p}}. \tag{3}$$

Since the plastic deformation is isochoric, $\det \boldsymbol{F}^{\mathrm{p}} = 1$.

The boundary value problem consists of equilibrium, neglecting body forces, on the reference configuration B_n

$$\nabla \cdot \boldsymbol{P}_r = 0 \tag{4}$$

and is subject to the boundary conditions

$$\begin{aligned} &\boldsymbol{u} = \bar{\boldsymbol{u}} \quad \text{on } \partial B_u, \\ &\boldsymbol{t} = \bar{\boldsymbol{t}} \quad \text{on } \partial B_t, \end{aligned} \tag{5}$$

where $\bar{\boldsymbol{u}}$ and $\bar{\boldsymbol{t}}$ are prescribed displacements and traction on ∂B_u and ∂B_t, respectively, and

$$\boldsymbol{P}_r = (\det \boldsymbol{F}_r)\boldsymbol{T}\boldsymbol{F}_r^{-\mathrm{T}} \tag{6}$$

is the first Piola–Kirchoff stress on B_n, $\boldsymbol{T}$ being the Cauchy stress on the deformed configuration B_{n+1}.

The constitutive model for the hyperelastic part of the deformation is assumed linear and isotropic

$$\widehat{\boldsymbol{T}} = \widehat{\mathscr{L}} : \widehat{\boldsymbol{E}}^{\mathrm{e}}, \tag{7}$$

where

$$\widehat{\mathscr{L}} = 2\mu\boldsymbol{\Pi} + \left(\kappa - \frac{2}{3}\mu\right)(\boldsymbol{I} \otimes \boldsymbol{I}), \tag{8}$$

$$\widehat{\boldsymbol{T}} = (\det \boldsymbol{F}^{\mathrm{e}})\boldsymbol{R}^{\mathrm{e}\mathrm{T}}\boldsymbol{T}\boldsymbol{R}^{\mathrm{e}} = (\det \boldsymbol{F})\boldsymbol{R}^{\mathrm{e}\mathrm{T}}\boldsymbol{T}\boldsymbol{R}^{\mathrm{e}}. \tag{9}$$

$\boldsymbol{I}$ and $\boldsymbol{\Pi}$ are the second- and fourth-order identity tensors, μ and κ being the shear and bulk modulus of the material and

$$\widehat{\boldsymbol{E}}^{\mathrm{e}} = \ln \boldsymbol{U}^{\mathrm{e}} \tag{10}$$

is the logarithmic strain. $\widehat{\boldsymbol{T}}$ is the stress measure that is work conjugate to the logarithmic strain for isotropic elasticity [10]. Furthermore, $\boldsymbol{R}^e$ and $\boldsymbol{U}^e$ are the rotation and right stretch tensors from the polar decomposition of $\boldsymbol{F}^e$. Using the elasticity relations, the mean stress $\hat{p}$ can be written as

$$\hat{p} = \frac{1}{3}\mathrm{tr}(\widehat{\boldsymbol{T}}) = \kappa\,\mathrm{tr}(\widehat{\boldsymbol{E}}) = \kappa\,\mathrm{tr}(\ln \boldsymbol{U}^{\mathrm{e}}) = \kappa \ln(\det \boldsymbol{U}^{\mathrm{e}}) = \kappa \ln(\det \boldsymbol{F}), \tag{11}$$

which results in the elastic compressibility condition

$$\ln(\det \boldsymbol{F}_r) - \frac{(\hat{p}_{n+1} - \hat{p}_n)}{\kappa} = 0. \tag{12}$$

The plastic part of the deformation gradient $\boldsymbol{F}^{\mathrm{p}}$ evolves according to the flow rule given by

$$\dot{\boldsymbol{F}}^{\mathrm{p}} = \widehat{\boldsymbol{L}}^{\mathrm{p}}\boldsymbol{F}^{\mathrm{p}} \tag{13}$$

with

$$\widehat{\boldsymbol{D}}^{\mathrm{p}} = \mathrm{sym}(\widehat{\boldsymbol{L}}^{\mathrm{p}}) = \sqrt{\frac{3}{2}}\dot{\bar{\varepsilon}}^{\mathrm{p}}\widehat{\boldsymbol{N}} \quad \text{and} \quad \widehat{\boldsymbol{W}}^{\mathrm{p}} = \mathrm{skw}(\widehat{\boldsymbol{L}}^{\mathrm{p}}) = 0, \tag{14}$$

where

$$\widehat{\boldsymbol{N}} = \sqrt{\frac{3}{2}}\frac{\widehat{\boldsymbol{T}}'}{\sigma} \tag{15}$$

is the direction of plastic flow, $\widehat{\boldsymbol{T}}' = \widehat{\boldsymbol{T}} - \frac{1}{3}\hat{p}\boldsymbol{I}$ is the deviatoric stress,

$$\sigma = \sqrt{\frac{3}{2}\widehat{\boldsymbol{T}}' \cdot \widehat{\boldsymbol{T}}'} \tag{16}$$

is the equivalent stress, and $\dot{\varepsilon}^{\mathrm{p}}$ is the equivalent plastic strain rate.

In the case of rate dependent viscoplasticity, $\dot{\varepsilon}^{\mathrm{p}}$ is prescribed by the constitutive function

$$\dot{\varepsilon}^{\mathrm{p}} = f(\sigma, s) \tag{17}$$

along with the evolution of the internal state variable s

$$\dot{s} = g(\dot{\varepsilon}^{\mathrm{p}}, s). \tag{18}$$

For rate independent plasticity, $\dot{\varepsilon}^{\mathrm{p}}$ is obtained from the consistency condition which requires that the stress state must stay on the yield surface $f = \sigma - (Y_0 + H\varepsilon^{\mathrm{p}})$ during plastic flow along with the associative flow rule

$$\widehat{\boldsymbol{D}}^{\mathrm{p}} = \dot{\varepsilon}^{\mathrm{p}}\frac{\partial f}{\partial \widehat{\boldsymbol{T}}}, \tag{19}$$

where Y_0 is the yield strength of the material and H is the isotropic hardening modulus. The stress update procedures for the constitutive models used herein are presented in Section 3.

3. Integration of constitutive equations

The procedure used for the time integration of the constitutive equations follows that outlined by Weber and Anand [32] and Eterovic and Bathe [6], and a summary is provided in Appendix A for completeness. The use of logarithmic strain causes the return mapping to be similar to that for small deformation plasticity. The integration procedure updates the Cauchy stress $\boldsymbol{T}$, internal state variable s and plastic deformation gradient $\boldsymbol{F}^{\mathrm{p}}$ over an increment Δt from t_n to t_{n+1} given the relative deformation gradient $\boldsymbol{F}_r$.

4. Stabilized formulation

Stabilized methods provide the freedom to choose interpolation functions based on accuracy and efficiency requirements without needing to be concerned about stability. Stabilized methods, as mentioned in Section 1, have been been used to overcome instabilities associated with incompressibility with much success in applications in fluid mechanics and incompressible, linear elasticity. For linear governing equations, the relationship to subscale methods [5,13] have been established and error estimates [12] have been derived. Recent works extending stabilized methods to non-linear problems in solid mechanics [14,17] have demonstrated promise and will be built upon herein.

Stabilized methods have the form of generalized Galerkin methods where mesh dependent terms, typically functions of the Euler–Lagrange equations (Eqs. (4) and (12)), are added to enhance the stability of the mixed method and circumvent the Babuška–Brezzi condition, thus allowing for greater flexibility in choosing the interpolation functions. In particular, the use of equal order interpolation for displacement and pressure (e.g. P1/P1) are supported by the present formulation. In this work, the push forward of the gradient of the pressure weighting function, $\boldsymbol{F}_r^{-\mathrm{T}}\nabla\tilde{p}$, ∇ being the gradient with respect to the reference coordinates $\boldsymbol{X}_n \in B_n$, is used to perturb the Galerkin weighting function. Thus, the strong form of the

equilibrium equation (4) is integrated with the weighting function $\tilde{\boldsymbol{w}} = \tilde{\boldsymbol{u}} + \delta \boldsymbol{F}_r^{-\mathrm{T}} \nabla \tilde{p}$ where $\tilde{\boldsymbol{u}}$ is the standard part and the second term is the perturbation, which gives rise to the stabilization terms. The coefficient δ is a mesh dependent stabilization parameter, which is chosen following Hughes et al. [11] as $\delta = \frac{\alpha h_e^2}{2\mu}$ where h_e is the characteristic element length, μ is the shear modulus of the material, and α is a non-dimensional, non-negative stability parameter. It should be noted that Hughes et al. [11] derived this form for the stabilization parameter for linear, small strain elasticity. The same form was found to work well for finite elasticity [14,17]. The same choice is used here; however, the range of "good" stabilization parameters is expected to be different from that in elasticity because the stress will be relaxed due to the plastic deformation. It is the relatively stiff elastic compressibility compared to the elastic–plastic distortion that leads to the instability in the elastic–plastic case. Thus, the stabilization parameter required to provide stability for the elastic–plastic case is expected to be higher than for the elastic case when scaled by the twice the elastic shear modulus. An alternative scaling is discussed in the results (Section 6). If α is chosen to be zero, the formulation reduces to the standard Galerkin formulation. In the absence of body forces, using the modified weighting function, the following Petrov–Galerkin formulation results. Find $\boldsymbol{u} \in U,\ \hat{p} \in P$ such that for all $\tilde{\boldsymbol{u}} \in V,\ \tilde{p} \in P$

$$\int_{B_n} (\nabla \cdot \boldsymbol{P}_r) \cdot \left(\tilde{\boldsymbol{u}} + \frac{\alpha h_e^2}{2\mu} \boldsymbol{F}_r^{-\mathrm{T}} \nabla \tilde{p} \right) \mathrm{d}V_n - \int_{B_n} \left[\ln(\det \boldsymbol{F}_r) - \frac{\hat{p}}{\kappa} \right] \tilde{p} \, \mathrm{d}V_n = 0, \tag{20}$$

is satisfied where

$$U = \left\{ \boldsymbol{u} \mid \boldsymbol{u} \in [H^1]^N, \boldsymbol{u} = \bar{\boldsymbol{u}} \text{ on } \partial B_u \right\},$$
$$V = \left\{ \boldsymbol{v} \mid \boldsymbol{v} \in [H^1]^N, \boldsymbol{v} = 0 \text{ on } \partial B_u \right\},$$
$$P = \{ p \mid p \in L^2 \}.$$

N being the space dimension and H^1 represents the Sobolev space. In Eq. (20), $\boldsymbol{u} = \boldsymbol{u}_{n+1} - \boldsymbol{u}_n$ and $\hat{p} = \hat{p}_{n+1} - \hat{p}_n$ represents the change in displacement and pressure over the increment and $\boldsymbol{F}_r = \boldsymbol{I} + \nabla \boldsymbol{u}$ is the relative deformation gradient.

Using Eqs. (6) and (66) along with the deviatoric split of $\widehat{\boldsymbol{T}}_{n+1} = \widehat{\boldsymbol{T}}'_{n+1} + (\hat{p}_n + \hat{p})\boldsymbol{I}$, the first Piola Kirchoff stress can be expressed as

$$\begin{aligned} \boldsymbol{P}_r &= \frac{(\det \boldsymbol{F}_r)}{(\det \boldsymbol{F}_{n+1})} \boldsymbol{R}_*^{\mathrm{e}} \widehat{\boldsymbol{T}}'_{n+1} \boldsymbol{R}_*^{\mathrm{e}\mathrm{T}} \boldsymbol{F}_r^{-\mathrm{T}} + \frac{(\det \boldsymbol{F}_r)}{(\det \boldsymbol{F}_{n+1})} (\hat{p}_n + \hat{p}) \boldsymbol{F}_r^{-\mathrm{T}} \\ &= (\det \boldsymbol{F}_r) \boldsymbol{T}'_{n+1} \boldsymbol{F}_r^{-\mathrm{T}} + (\det \boldsymbol{F}_r)(p_n + p) \boldsymbol{F}_r^{-\mathrm{T}}, \end{aligned} \tag{21}$$

where

$$p_{n+1} = \frac{1}{3} \mathrm{tr}(\boldsymbol{T}_{n+1}) = \frac{\hat{p}_{n+1}}{\det \boldsymbol{F}_{n+1}}.$$

The divergence of $\boldsymbol{P}_r$ becomes

$$\begin{aligned} \nabla \cdot \boldsymbol{P}_r &= \nabla \cdot [(\det \boldsymbol{F}_r) \boldsymbol{T}'_{n+1} \boldsymbol{F}_r^{-\mathrm{T}}] + (\det \boldsymbol{F}_r) \nabla (p_n + p) \boldsymbol{F}_r^{-\mathrm{T}} \\ &= (\det \boldsymbol{F}_r)[\nabla \cdot \boldsymbol{T}'_n + \nabla \cdot (\boldsymbol{T}'_{n+1} - \boldsymbol{T}'_n)] \boldsymbol{F}_r^{-\mathrm{T}} + (\det \boldsymbol{F}_r) \nabla (p_n + p) \boldsymbol{F}_r^{-\mathrm{T}} \\ &= (\det \boldsymbol{F}_r)[\nabla \cdot (\boldsymbol{T}'_{n+1} - \boldsymbol{T}'_n)] \boldsymbol{F}_r^{-\mathrm{T}} + (\det \boldsymbol{F}_r) \nabla p \boldsymbol{F}_r^{-\mathrm{T}} \\ &= \nabla \cdot [(\det \boldsymbol{F}_r)(\boldsymbol{T}'_{n+1} - \boldsymbol{T}'_n) \boldsymbol{F}_r^{-\mathrm{T}}] + (\det \boldsymbol{F}_r) \nabla p \boldsymbol{F}_r^{-\mathrm{T}}, \end{aligned} \tag{22}$$

where the Piola identity $\nabla \cdot [(\det \boldsymbol{F}_r) \boldsymbol{F}_r^{-\mathrm{T}}] = 0$ and $\nabla \cdot (\boldsymbol{T}'_n + p_n \boldsymbol{I}) = 0$ were used to arrive at the above result. Integrating the first term in Eq. (20) by parts and assuming $p \approx \hat{p}$ due to the near incompressibility ($\det \boldsymbol{F}_{n+1} \approx 1$) gives

$$-\int_{B_n} \boldsymbol{P}_r : \nabla\tilde{\boldsymbol{u}}\,\mathrm{d}V_n + \int_{\partial B_n} \boldsymbol{t}_r \cdot \tilde{\boldsymbol{u}}\,\mathrm{d}A_n + \int_{B_n} (\nabla \cdot \boldsymbol{P}_r) \cdot \frac{\alpha h_e^2}{2\mu} (\boldsymbol{F}_r^{-\mathrm{T}} \nabla\tilde{p})\,\mathrm{d}V_n - \int_{B_n} \left[\ln(\det \boldsymbol{F}_r) - \frac{p}{\kappa}\right]\tilde{p}\,\mathrm{d}V_n = 0. \tag{23}$$

Considering the arbitrariness of the weight functions $\tilde{\boldsymbol{u}}$ and $\tilde{p}$ and substituting for $\nabla \cdot \boldsymbol{P}_r$ from Eq. (22) leads to the following stabilized mixed weak formulation

$$\int_{B_n} \boldsymbol{P}_r : \nabla\tilde{\boldsymbol{u}}\,\mathrm{d}V_n = \int_{\partial B_n} \boldsymbol{t}_r \cdot \tilde{\boldsymbol{u}}\,\mathrm{d}A_n, \tag{24}$$

$$\int_{B_n} \left[\ln(\det \boldsymbol{F}_r) - \frac{p}{\kappa}\right]\tilde{p}\,\mathrm{d}V_n - \sum_{e=1}^{n_{\mathrm{el}}} \frac{\alpha h_e^2}{2\mu} \int_{B_n^{\mathrm{e}}} [(\det \boldsymbol{F}_r)\boldsymbol{F}_r^{-1}\boldsymbol{F}_r^{-\mathrm{T}}] : [\nabla p \otimes \nabla\tilde{p}]\,\mathrm{d}V_n^{\mathrm{e}}$$
$$- \sum_{e=1}^{n_{\mathrm{el}}} \frac{\alpha h_e^2}{2\mu} \int_{B_n^{\mathrm{e}}} \left\{\nabla \cdot [(\det \boldsymbol{F}_r)(\boldsymbol{T}'_{n+1} - \boldsymbol{T}'_n)\boldsymbol{F}_r^{-\mathrm{T}}]\right\} \cdot (\boldsymbol{F}_r^{-\mathrm{T}} \nabla\tilde{p})\,\mathrm{d}V_n^{\mathrm{e}} = 0, \tag{25}$$

where n_{el} is the number of elements and the perturbation is applied element-wise. It should be noted that for linear interpolation of the displacement field (triangles or tetrahedra), the last term in Eq. (25) is zero. By allowing for linear interpolation of both the displacement and pressure fields, the number of degrees of freedom is greatly reduced from the quadratic displacement interpolation functions (on triangles and tetrahedra) required by the Babuška-Brezzi condition. However, for higher order interpolations, $\nabla \cdot [(\det \boldsymbol{F}_r)(\boldsymbol{T}'_{n+1} - \boldsymbol{T}'_n)\boldsymbol{F}_r^{-\mathrm{T}}]$ is not zero and depends in a complicated way on the gradient of the displacement field. Maniatty et al. [18] use a local reconstruction method to compute this term and treat the last term in Eq. (25) as a forcing term by moving it to the right-hand side in order to avoid computing the complex derivatives required for linearization.

For discontinuous pressure elements an additional stabilization term

$$-\sum_{e=1}^{n_{\mathrm{el}}} \frac{\beta h_e}{2\mu} \widetilde{\Gamma} \int [\![p]\!][\![\tilde{p}]\!]\,\mathrm{d}A$$

has to be added [12] to Eq. (25) where $[\![p]\!]$ denotes the jump in pressure across the interelement boundary $\widetilde{\Gamma}$ and β is another nondimensional stability parameter. Due to coupling between elements, the pressure cannot be eliminated at the element level and does not offer any advantages compared to continuous pressure elements. Franca et al. [7] show that these terms are unnecessary if the interpolation order $k \geqslant 2$ in two dimensions and $k \geqslant 3$ in three dimensions for triangles and tetrahedra, where k is the order of interpolation of the displacement field. This allows the nodal pressures to be eliminated at the element level using a penalty technique. However, since we are focusing on stabilizing linear P1/P1 elements, we restrict ourselves to continuous pressure elements and

$$P = \{p \mid p \in C^0\},$$

where C^0 implies a continuous function.

5. Linearization

A Newton–Raphson algorithm is used to solve the system of equations (24) and (25). Consistent linearization is necessary to preserve quadratic convergence. Linearization leads to the stabilized system of equations

$$\begin{aligned} K_{(\boldsymbol{u},p)}(\tilde{\boldsymbol{u}},\Delta\boldsymbol{u}) + G_{(\boldsymbol{u})}(\tilde{\boldsymbol{u}},\Delta p) &= f(\tilde{\boldsymbol{u}}) - k_{(\boldsymbol{u},p)}(\tilde{\boldsymbol{u}}), \\ H_{(\boldsymbol{u},p)}(\tilde{p},\Delta\boldsymbol{u}) + M_{(\boldsymbol{u})}(\tilde{p},\Delta p) &= \mathscr{H}_{(\boldsymbol{u})}(\tilde{p}) - h_{(\boldsymbol{u},p)}(\tilde{p}), \end{aligned} \tag{26}$$

where

$$k_{(\boldsymbol{u},p)}(\tilde{\boldsymbol{u}}) = \int_{B_n} \boldsymbol{P}_r : \nabla\tilde{\boldsymbol{u}}\,\mathrm{d}V_n, \tag{27}$$

$$f(\tilde{\boldsymbol{u}}) = \int_{\partial B_n} \boldsymbol{t}_r \cdot \tilde{\boldsymbol{u}}\,\mathrm{d}A_n, \tag{28}$$

$$h_{(\boldsymbol{u},p)}(\tilde{p}) = \int_{B_n} \left[\ln(\det \boldsymbol{F}_r) - \frac{p}{\kappa}\right]\tilde{p}\,\mathrm{d}V_n - \sum_{e=1}^{n_{\mathrm{el}}} \frac{\alpha h_e^2}{2\mu} \int_{B_n^{\mathrm{e}}} [(\det \boldsymbol{F}_r)\boldsymbol{F}_r^{-1}\boldsymbol{F}_r^{-\mathrm{T}}] : [\nabla\tilde{p} \otimes \nabla p]\,\mathrm{d}V_n^{\mathrm{e}}, \tag{29}$$

$$\mathscr{H}_{(\boldsymbol{u})}(\tilde{p}) = \sum_{e=1}^{n_{\mathrm{el}}} \frac{\alpha h_e^2}{2\mu} \int_{B_n^{\mathrm{e}}} \left\{\nabla \cdot [(\det \boldsymbol{F}_r)(\boldsymbol{T}'_{n+1} - \boldsymbol{T}'_n)\boldsymbol{F}_r^{-\mathrm{T}}]\right\} \cdot (\boldsymbol{F}_r^{-\mathrm{T}}\nabla\tilde{p})\,\mathrm{d}V_n^{\mathrm{e}} \tag{30}$$

with $\boldsymbol{P}_r$ as defined in Eq. $(21)_1$.

$$K_{(\boldsymbol{u},p)}(\tilde{\boldsymbol{u}},\Delta\boldsymbol{u}) = D_{\boldsymbol{u}}[k_{(\boldsymbol{u},p)}(\tilde{\boldsymbol{u}})]\Delta\boldsymbol{u} = \int_{B_n} \nabla\tilde{\boldsymbol{u}} : D_{\boldsymbol{u}}[\boldsymbol{P}_r(\boldsymbol{u},p)]\Delta\boldsymbol{u}\,\mathrm{d}V_n, \tag{31}$$

$$G_{(\boldsymbol{u})}(\tilde{\boldsymbol{u}},\Delta p) = D_p[k_{(\boldsymbol{u},p)}(\tilde{\boldsymbol{u}})]\Delta p = \int_{B_n} \frac{1}{(\det \boldsymbol{F}_n)} \mathrm{tr}(\boldsymbol{F}_r^{-1}\nabla\tilde{\boldsymbol{u}})\Delta p\,\mathrm{d}V_n, \tag{32}$$

$$\begin{aligned} H_{(\boldsymbol{u},p)}(\tilde{p},\Delta\boldsymbol{u}) = D_{\boldsymbol{u}}[h_{(\boldsymbol{u},p)}(\tilde{p})]\Delta\boldsymbol{u} = &\int_{B_n} \tilde{p}\,\mathrm{tr}[\boldsymbol{F}_r^{-1}\nabla(\Delta\boldsymbol{u})]\,\mathrm{d}V_n \\ &- \sum_{e=1}^{n_{\mathrm{el}}} \frac{\alpha h_e^2}{2\mu} \int_{B_n^{\mathrm{e}}} (\det \boldsymbol{F}_r)\Big\{\mathrm{tr}[\boldsymbol{F}_r^{-1}\nabla(\Delta\boldsymbol{u})]\boldsymbol{F}_r^{-1}\boldsymbol{F}_r^{-\mathrm{T}} - \boldsymbol{F}_r^{-1}\nabla(\Delta\boldsymbol{u})\boldsymbol{F}_r^{-1}\boldsymbol{F}_r^{-\mathrm{T}} - \boldsymbol{F}_r^{-1}\boldsymbol{F}_r^{-\mathrm{T}}[\nabla(\Delta\boldsymbol{u})]^{\mathrm{T}}\boldsymbol{F}_r^{-\mathrm{T}}\Big\} \\ &: [\nabla\tilde{p} \otimes \nabla p]\,\mathrm{d}V_n^{\mathrm{e}}, \end{aligned} \tag{33}$$

$$\begin{aligned} M_{(\boldsymbol{u})}(\tilde{p},\Delta p) = D_p[h_{(\boldsymbol{u},p)}(\tilde{p})]\Delta p = &-\int_{B_n} \frac{1}{\kappa}\tilde{p}\Delta p\,\mathrm{d}V_n \\ &- \sum_{e=1}^{n_{\mathrm{el}}} \frac{\alpha h_e^2}{2\mu} \int_{B_n^{\mathrm{e}}} [(\det \boldsymbol{F}_r)\boldsymbol{F}_r^{-1}\boldsymbol{F}_r^{-\mathrm{T}}] : [\nabla\tilde{p} \otimes \nabla(\Delta p)]\,\mathrm{d}V_n^{\mathrm{e}}, \end{aligned} \tag{34}$$

where $D_\phi[A(\phi)]\Delta\phi$ represents the directional derivative of A in the direction $\Delta\phi$. Note that for linear interpolation of the displacement field, $\mathscr{H}_{(\boldsymbol{u})}(\tilde{p}) = 0$. For higher order interpolations, this term could be reconstructed using the procedure given in [18] and treated as a forcing term. The linearization of the first Piola–Kirchoff stress $\boldsymbol{P}_r$, required in Eq. (31), is given in Appendix B.

6. Numerical examples

In order to test the behavior of the proposed, stabilized, mixed finite element formulation with P1/P1 elements (which does not satisfy the Babuška–Brezzi condition) in the presence of plastic incompressibility, four examples are considered: expansion of a thick cylinder, extension of a plate with a flat hole, Cook's plane strain problem, and the upsetting of a cylindrical billet. The examples are chosen such that the mate-

rial is highly constrained causing instability in the nearly incompressible limit unless stabilization is applied, demonstrating the effectiveness of the present formulation. The constitutive laws considered include both rate independent plasticity and rate dependent viscoplasticity. The case of expansion of a thick cylinder is used to study the effect of the stabilization parameter, the mesh refinement, and the "time" step refinement on the convergence and accuracy of the method. For the other examples, comparisons are made with stable elements and with previously published results. Convergence is said to be achieved when the residual is reduced by a factor of 10^{-6}. In some cases, results with unstable elements are presented with a different colormap as their results usually deteriorate causing much larger extreme values compared to the stable elements. The meshes are generated using the T3d generator developed by Rypl [25].

6.1. Expansion of a thick cylinder

In this example, a cylinder of initial inner radius $R_i = 1$ m and outer radius $R_o = 2$ m is subjected to plane strain expansion where the final inner radius is expanded out to $r_i = 1.5$ m. Using symmetry boundary conditions, a quarter of the cylinder is modeled. The material was chosen to be elastic–plastic with a shear modulus $\mu = 76.92$ MPa, bulk modulus $\kappa = 166.67$ MPa, yield stress $Y_0 = 0.3$ MPa and a linear isotropic hardening modulus $H = 0.7$ MPa. An approximate analytic solution to this problem, neglecting the relatively small elastic deformations, is

$$D^{\mathrm{p}}_{rr} = -\frac{r_i \dot{r}_i}{r^2} \quad D^{\mathrm{p}}_{\theta\theta} = \frac{r_i \dot{r}_i}{r^2}, \tag{35}$$

$$\epsilon^{\mathrm{p}} = \frac{1}{\sqrt{3}} \ln\left(\frac{r^2 + R_i^2 + 2R_i r_i}{r^2 + R_i^2 - r_i^2}\right), \tag{36}$$

$$\sigma = Y_o + H\epsilon^{\mathrm{p}} \quad T'_{rr} = -\frac{\sigma}{\sqrt{3}} \quad T'_{\theta\theta} = \frac{\sigma}{\sqrt{3}}, \tag{37}$$

$$\frac{\partial p}{\partial r} = -\frac{\partial T'_{rr}}{\partial r} - 2\frac{T'_{rr}}{r} \tag{38}$$

where r represents the radial position in the deformed cylinder. Substituting Eqs. (37) and (36) into Eq. (38) results in an equation that can be integrated numerically for the pressure using the boundary condition $T_{rr}(r_o) = T'_{rr}(r_o) + p(r_o) = 0$. The pressure can then be added to the deviatoric stress components to give the total stress. This solution is used to validate the finite element model. The effect of the stabilization parameter, mesh refinement, and step size on the accuracy and convergence behavior is investigated.

First, the effect of the stabilization parameter is studied. A mesh with 400 P1/P1 elements with 231 nodes (3 degrees of freedom (d.o.f.) per node, 2 displacement, 1 pressure) is considered, and the expansion is done in 10 equal increments. An error measure on the radial stress T_{rr} of the following form is used

$$\text{Error} = \frac{1}{T^A_{rr}(r_i)} \sqrt{\frac{1}{N_{\text{int}}} \sum_{\text{int}=1}^{N_{\text{int}}} (T^{\text{int}}_{rr} - T^{A(\text{int})}_{rr})^2} \tag{39}$$

where T^{int}_{rr} and $T^{A(\text{int})}_{rr}$ are the computed and analytic radial stress components at the finite element integration points, respectively. Fig. 1 shows the effect of the stabilization parameter on the error. The results are insensitive to the stabilization parameter for $\alpha > 10$ and values between 10^2 and 10^4 appear to be optimal. The other components of the stress were also found to have similar accuracy. Figs. 2 and 3 show the contour plots of T_{rr} using P1/P1 elements with and without stabilization for a stabilization parameter $\alpha = 100$. Without stabilization, the results are very poor with strong spatial oscillations appearing in the solution.

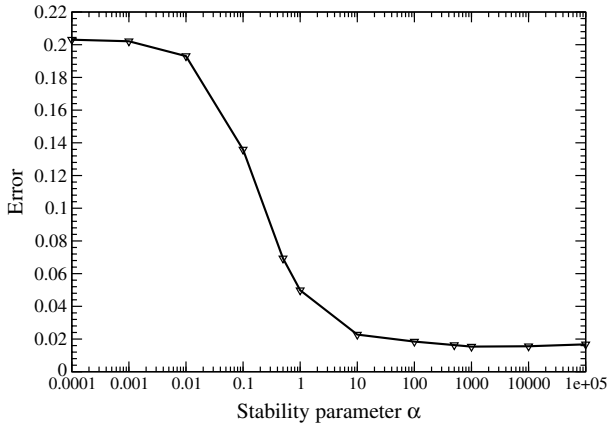

Fig. 1. Effect of the stabilization parameter, α, on the error.

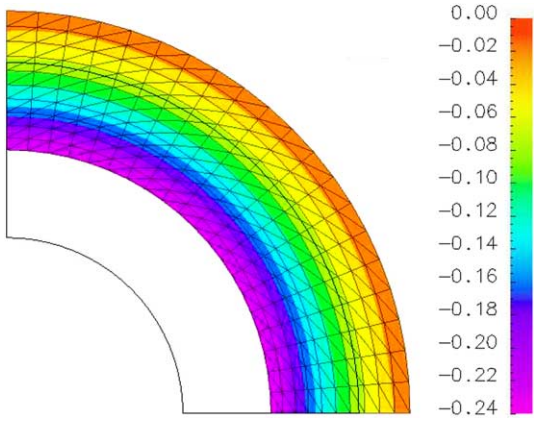

Fig. 2. Contours of stress component T_{rr} in MPa with stabilization, $\alpha = 100$.

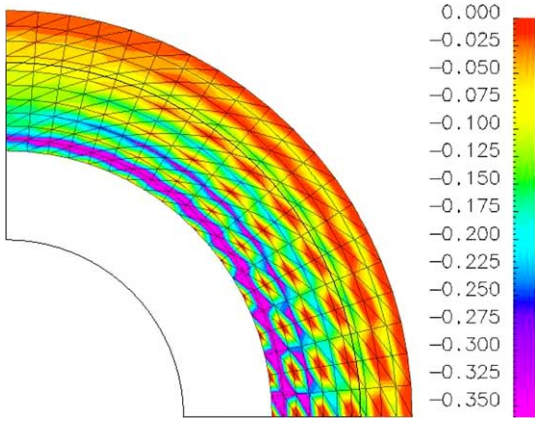

Fig. 3. Contours of stress component T_{rr} in MPa without stabilization.

It should be noted that a higher value of the stability parameter α is required to suppress oscillations in the presence of plastic incompressibility compared to incompressible hyperelasticity, for example, in Klaas et al. [14] and Maniatty et al. [18] where $\alpha = 1$ was found to work well. This is likely because of the scaling of α with twice the elastic shear modulus, 2μ, in Eq. (20), which, while appropriate for elastic behavior, is too large for elastic–plastic behavior where the stress is relaxed due to the plasticity. While the elastic part of the behavior governs the compressible part of the deformation, it is the relationship between the relatively stiff elastic compressibility and the relatively soft elastic–plastic distortion which causes the instability. A different scaling that may be proposed is to use the elastic–plastic material stiffness derived in the consistent linearization. Considering Eq. (75), the scaling parameter analogous to 2μ in the elastic case would be

$$2\mu\left(1 - 3\mu\frac{\Delta\epsilon^{\mathrm{p}}}{\sigma^*}\right) \tag{40}$$

for the elastic–plastic case, and using Eq. (53) results in

$$2\mu\left(\frac{\sigma_{n+1}}{\sigma_{n+1} + 3\mu\Delta\epsilon^{\mathrm{p}}}\right), \tag{41}$$

which, for a large plastic increment ($\Delta\epsilon^{\mathrm{p}} = \mathrm{O}(0.1)$ in this case) would give a scaling parameter of roughly $0.01 \times 2\mu$, and thus, an optimal stabilization parameter scaled by this parameter would be in the range of 1–10^2, consistent with that found in elasticity. The important point to note, however, is that the solution is insensitive to the stabilization parameter over a broad range of values, and once a value is chosen that suppresses oscillations, that parameter appears to work for a wide variety of meshes and problems, as will be shown.

Next, the effect of mesh refinement and step size and the convergence behavior are investigated. For these studies, the sensitivity parameter is held fixed at $\alpha = 100$. Fig. 4 shows the effect of mesh refinement on the accuracy for a fixed step size of 10 equal increments. The usual h-convergence behavior is observed. Varying the number of increments, or in other words, varying the "pseudo-time" step size, was also investigated. The results for 3, 5, 10, 20, 50 and 100 increments varied by less than 5%, and the difference between the results for 10 and 100 increments varied by less than 2%, with the error going down slightly as the number of increments increased. This is not surprising because the deformation path does not change with time, i.e. the principle directions of the deformation are fixed, so a large step size can capture the whole deformation history well. Finally, to demonstrate the convergence of the linearized system, the number of

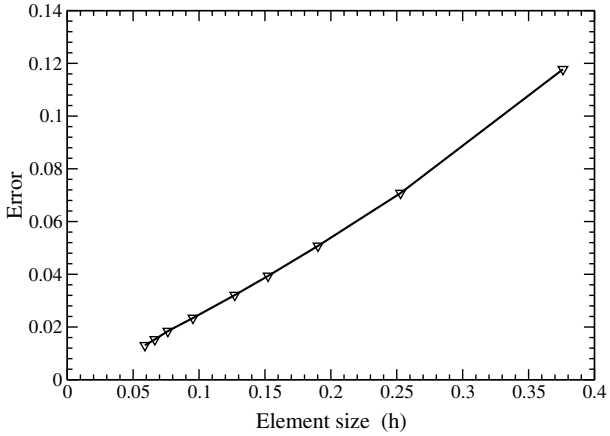

Fig. 4. Effect of mesh size on the error for the thick cylinder example.

Table 1
Number of iterations for different increments for the expansion of a thick cylinder example

Increment	1	2–10
Number of iterations	4	3

iterations to convergence for each increment is given in Table 1. The Newton-Raphson algorithm was found to converge quadratically.

6.2. Plate with a flat hole

The example of a square plate with a flat hole in plane strain is considered. The geometry and boundary conditions are as shown in Fig. 5. A displacement boundary condition is applied stretching the plate by 3%. Only a quarter of the plate is modeled and symmetry conditions are applied. The material is modeled as elastic–plastic with the same material parameters as in the previous thick cylinder example (shear modulus $\mu = 76.92$ MPa, bulk modulus $\kappa = 166.67$ MPa, yield stress $Y_0 = 0.3$ MPa, hardening modulus $H = 0.7$ MPa).

The mesh consists of 224 nodes (3 d.o.f. per node) and 393 P1/P1 triangles with linear interpolation for displacement and pressure fields. Calculations were performed with the non-dimensional stability parameter $\alpha = 100$. This solution is compared to that obtained using the a priori stable P2/P0 triangular elements with quadratic interpolation of the displacement and constant pressure on a fixed finite element mesh. It should be noted that since the pressure is discontinuous for P2/P0 elements, the pressure can be easily eliminated on the element level, and thus, is not solved for directly. The mesh with P2/P0 elements consists of 840 nodes (2 d.o.f. per node, 2 displacement) and 393 triangles.

The axial component of the Cauchy stress field T_{22} computed with stable P2/P0 elements is shown in Fig. 6 and with P1/P1 elements without stabilization in Fig. 7. The P1/P1 element without stabilization performs poorly, exhibiting oscillations in the stress field as expected. The results with P2/P0 elements are chosen as the reference solution since these elements are inherently stable. Fig. 8 shows the stress field with the sta-

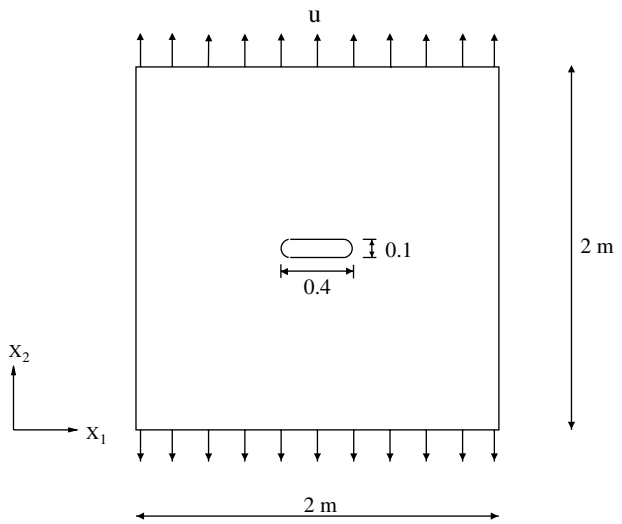

Fig. 5. Plane strain plate with a hole geometry.

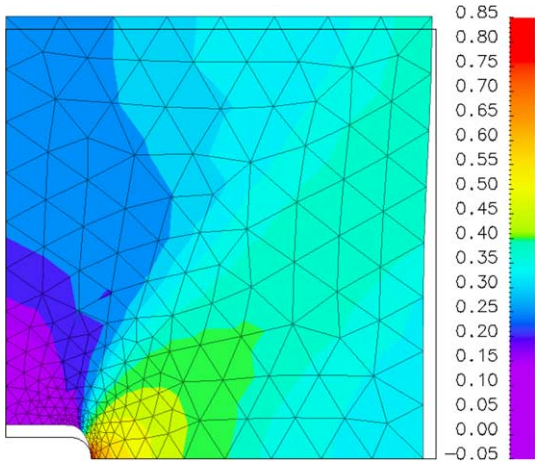

Fig. 6. Stress T_{22} in MPa with stable P2/P0 elements.

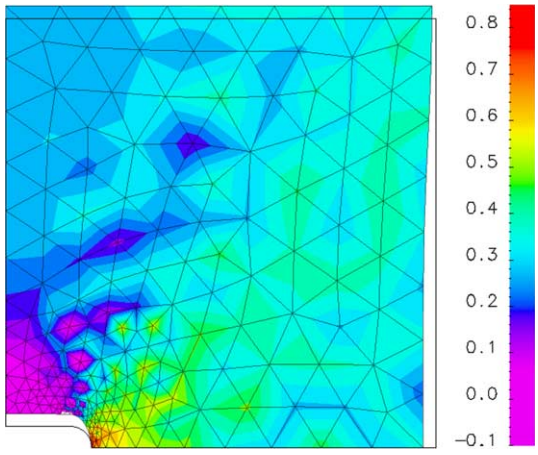

Fig. 7. Stress T_{22} in MPa with P1/P1 elements without stabilization.

bilized P1/P1 elements. The results of the stable P1/P1 elements compare favorably to that of P2/P0 elements. The stabilized P1/P1 elements have a total d.o.f of 672 in comparison to 1680 with the stable P2/P0 elements. Thus, the use of linear elements with stabilization leads to a significant reduction in the number of d.o.f. This reduction is expected to be more significant in 3D (see for example [18]).

6.3. Cook's plane strain problem

This problem has been used by many authors (see Brink and Stein [2], Klaas et al. [14]) to test new finite element formulations under combined bending and shear. A tapered panel is clamped on one side while a shearing displacement acts on the other side (Fig. 9). A vertical displacement $u = 7$ mm was applied to all the nodes on side BC as shown in the figure. Again, the material was chosen to be elastic–plastic with the same properties as in the prior two examples (shear modulus $\mu = 76.92$ MPa, bulk modulus $\kappa = 166.67$ MPa, yield stress $Y_0 = 0.3$ MPa, hardening modulus $H = 0.7$ MPa).

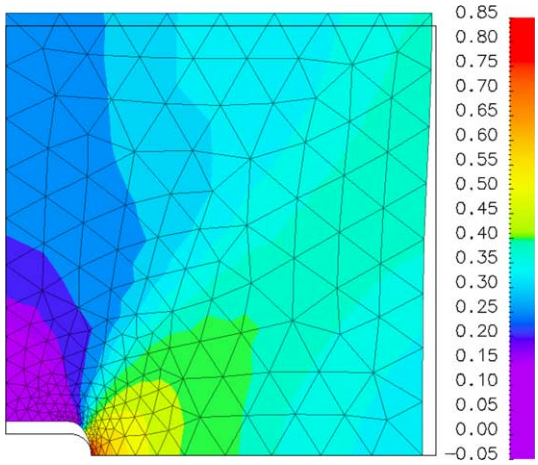

Fig. 8. Stress T_{22} in MPa with P1/P1 elements with stabilization, $\alpha = 100$.

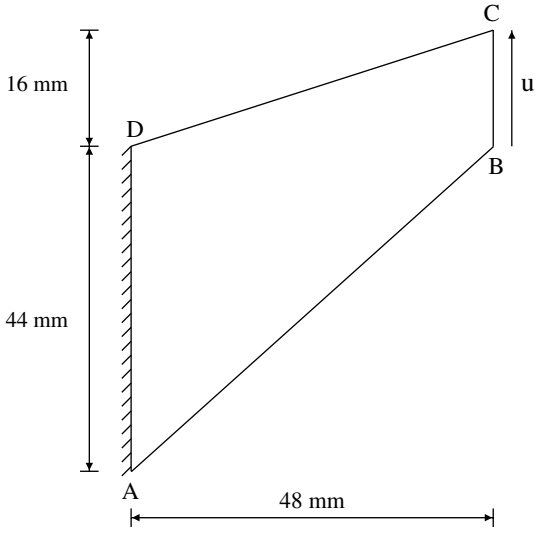

Fig. 9. Cook's plane strain problem.

Calculations were performed with the non-dimensional stability parameter $\alpha = 100$. Figs. 10–12 show the first principal stresses using P2/P0 elements, P1/P1 elements and P1/P1 elements with stabilization. As in the previous example, the P1/P1 elements without stabilization performs poorly. The P2/P0 and the P1/P1 stabilized elements give similar solutions when comparing Figs. 10 and 12. Table 2 provides a comparison of the maximum and minimum principal stresses for all three cases. The minimum values of the principal stresses occur at the top corner where the panel is clamped. The P2/P0 element is more effective in capturing the stress concentration here due to the higher order of the displacements. A fixed mesh with 847 elements was used to compare the results. The mesh with P1/P1 elements had 473 nodes (1419 d.o.f) while the mesh with P2/P0 elements had 1792 nodes (3584 d.o.f). Table 3 lists the number of degrees of freedom used in both the previous and the current examples.

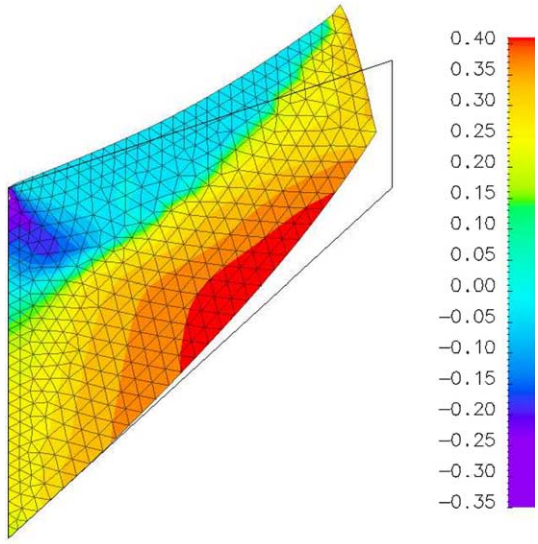

Fig. 10. First principal stress in MPa for P2/P0 elements.

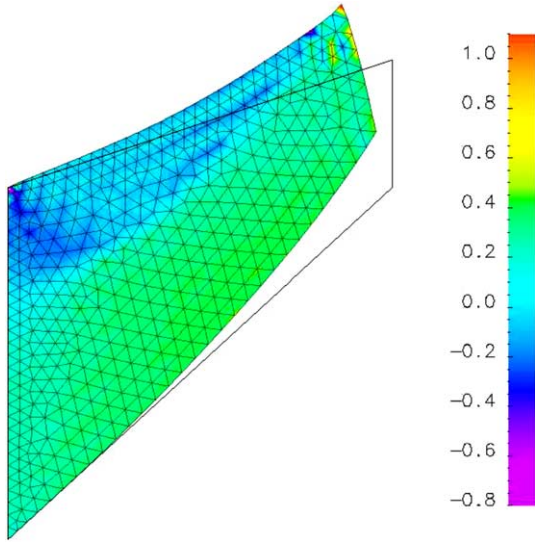

Fig. 11. First principal stress in MPa for P1/P1 elements without stabilization.

6.4. Upset forging of aluminum

The simulation of isothermal upset forging of an aluminum billet at a nominal strain rate of 0.01 s^{-1} was carried out and compared to the results presented in Weber and Anand [32] and Lush et al. [16]. The viscoplastic constitutive equations for hot working of metals developed by Brown et al. [3] is used. The behavior is highly nonlinear with the flow function and evolution equation as follows:

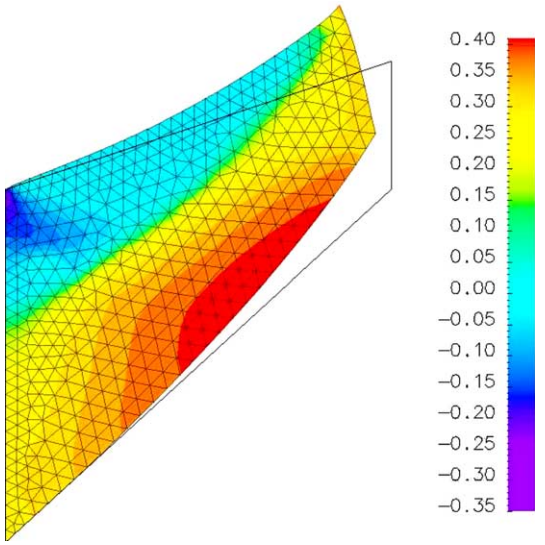

Fig. 12. First principal stress in MPa for P1/P1 elements with stabilization, $\alpha = 100$.

Table 2
Comparison of principal stresses for Cook's plane strain problem

	σ_1		σ_2		σ_3	
	Max	Min	Max	Min	Max	Min
P2/P0	0.457	−0.348	0.231	−0.577	0.031	−0.753
Stabilized P1/P1	0.439	−0.233	0.215	−0.310	0.013	−0.615
P1/P1	0.958	−0.722	0.742	−0.834	0.535	−1.076

Table 3
Number of degrees of freedom

	Degrees of freedom		
	Displacement	Pressure	Total
Plate with hole			
P2/P0	1680	0	1680
P1/P1	448	224	672
Cook's plane strain			
P2/P0	3584	0	3584
P1/P1	946	473	1419

$$\dot{\varepsilon}^{\mathrm{p}} = f(\sigma, s) = \overline{A}\left[\sinh\left(\xi\frac{\sigma}{s}\right)\right]^{1/m}, \tag{42}$$

$$\dot{s} = g(\dot{\varepsilon}^{\mathrm{p}}, s) = \left[h_0\left|1 - \frac{s}{s^{\star}}\right|^{a}\operatorname{sign}\left(1 - \frac{s}{s^{\star}}\right)\right]\dot{\varepsilon}^{\mathrm{p}}, \tag{43}$$

where $s^{\star} = \tilde{s}\left\{\dfrac{\dot{\varepsilon}^{\mathrm{p}}}{\overline{A}}\right\}^{n}$

Table 4
Material parameters for 1100 Al at 450 °C

Material parameter	Value
$\overline{A}$	4.73×10^{-3} s^{-1}
ξ	7.0
m	0.23348
s_0	29.7 MPa
h_0	1115.6 MPa
a	1.3
$\tilde{s}$	18.9 MPa
n	0.07049
μ	20.2 GPa
κ	66.0 GPa

and $\overline{A}$, ξ, m, h_0, $\tilde{s}$, a, n are material parameters (Table 4) for 1100 Al at 450 °C and are chosen as in [3]. Parameter s is a state variable representing the isotropic deformation resistance.

Two different deformations of the cylindrical billet, with a diameter of 12.7 mm and a height of 19.05 mm, are considered. Symmetry allows the modeling of one-fourth of the billet. A node-to-segment contact algorithm [30,33] is used to model the contact interactions between the die and billet. The die is considered to be rigid and sticking friction is assumed between the die and the billet. The adaptive time stepping procedure of Lush et al. [16] is used to control the motion of the die and is crucial in the case of very large deformations when new nodes come into contact with the die. The stress field for 30% upsetting with unstable and stabilized P1/P1 elements are compared while the die forces, effective plastic strain and the hardening, represented by the evolution of the state variable s, are compared to that obtained by Lush et al. for 60% upsetting. The effect of the stabilization parameter is again investigated for this different material model.

The mesh for 30% upsetting with P1/P1 elements consists of 121 nodes and 100 triangular elements. The Cauchy stress along the compression axis, T_{22}, for P1/P1 elements without stabilization is shown in Fig. 13. This element shows the checkerboard oscillations for the pressure, rendering the solution useless. To show the effect of the stabilization parameter, the component of the stress field for the stabilized P1/P1 element is shown in Figs. 14 and 15 with $\alpha = 10$ and $\alpha = 1000$, respectively. With $\alpha = 10$, some oscillations in the stress field are still evident, while $\alpha = 1000$ produces a smooth and stable stress field. A plot of the pressure on the

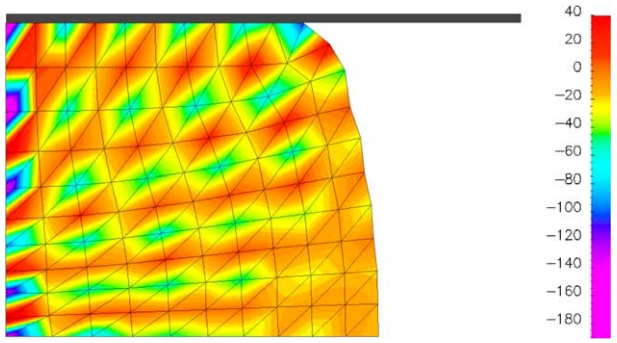

Fig. 13. Stress T_{22} in MPa for P1/P1 elements without stabilization.

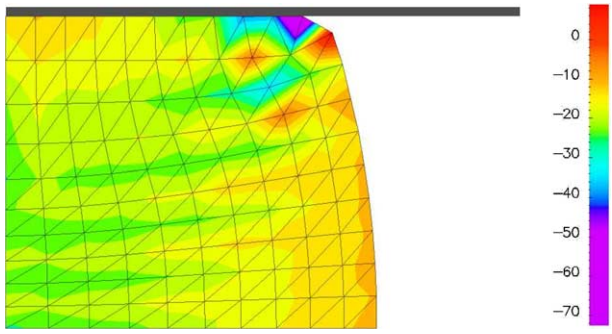

Fig. 14. Stress T_{22} in MPa for P1/P1 elements with stabilization ($\alpha = 10$).

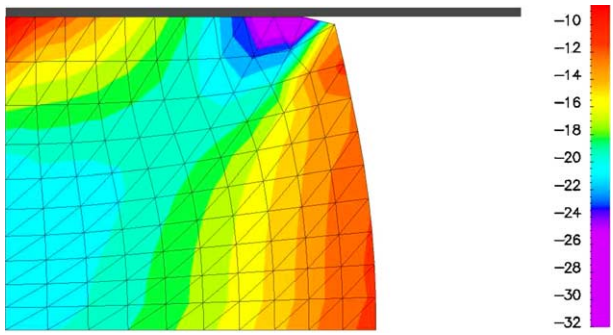

Fig. 15. Stress T_{22} in MPa for P1/P1 elements with stabilization ($\alpha = 1000$).

element located at the center of the billet and in contact with the die at the end of the stroke, where the pressure is maximum, is shown in Fig. 16 for different values of the stability parameter α. It was seen that a value of α between 10^2 and 10^4 was effective in suppressing oscillations in pressure and provides results comparable to known stable elements. Computing the scaling parameter proposed in Eq. (41) for this case gives a similar value as before of roughly $0.01 \times 2\mu$, which explains why the "good" values for α for this example happen to be in the same range as for the previous examples. As before, it is expected that once

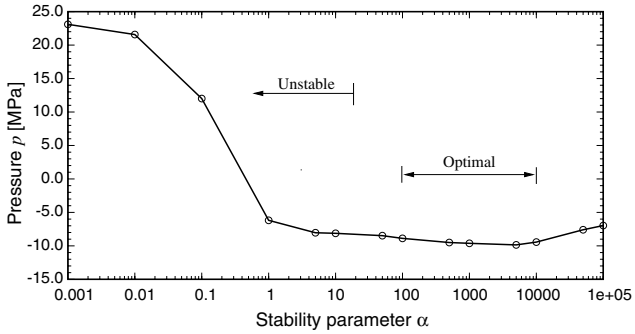

Fig. 16. Effect of the stabilization parameter α on the maximum pressure for the upset forging example.

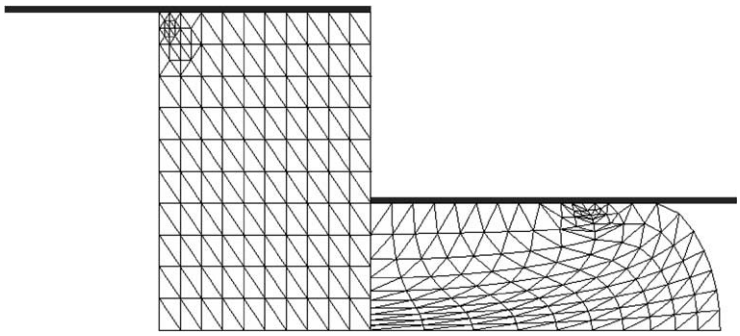

Fig. 17. Undeformed and deformed mesh for axisymmetric upsetting (60%).

a stability parameter has been found that suppresses oscillations for a given material model, no further calibration is necessary as the value of α does not seem to be problem dependent. Therefore, $\alpha = 1000$ was chosen for the next case with larger deformation (60% upsetting). The height of the billet was reduced by 60% in 90 s. The simulation took 101 increments with the time stepping prescribed by the adaptive algorithm. Fig. 17 shows the undeformed and deformed meshes for this case. The effective stress and the pressure field after deformation are shown in Figs. 18 and 19, respectively. The pressure field is smooth showing that the stabilization technique is effective in suppressing the oscillations. The effective plastic strain (Fig. 20)

$$\varepsilon^{\mathrm{p}} = \int_0^t \dot{\varepsilon}^{\mathrm{p}}\,\mathrm{d}t \tag{44}$$

and the state variable fields (Fig. 21) are similar to the ones published in Lush et al. [16]. Fig. 22 shows the total die force versus the die displacement. The die force calculated is in agreement with the experimental data and simulations performed by Weber and Anand [32]. A jump in the die force occurs when new nodes

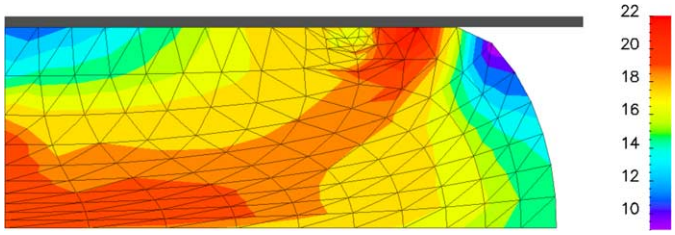

Fig. 18. Contours of the effective stresses in MPa.

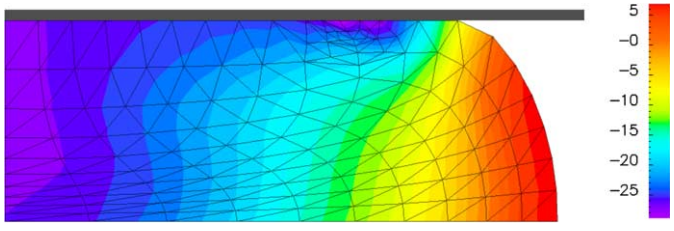

Fig. 19. Contours of the pressure in MPa.

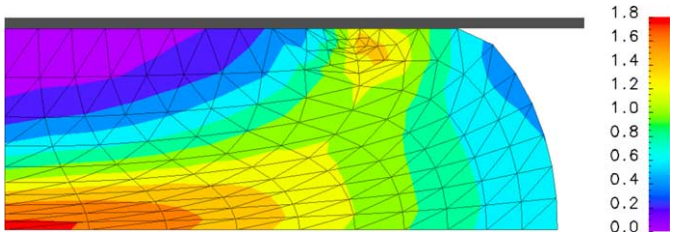

Fig. 20. Contours of the effective plastic strain.

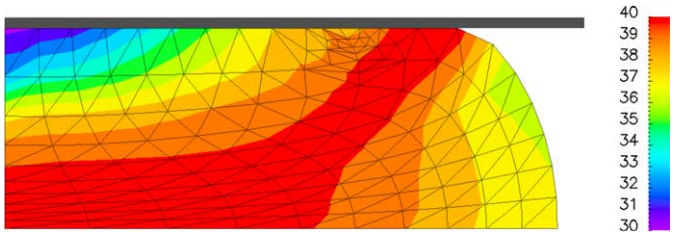

Fig. 21. Contours of the state variable s in MPa.

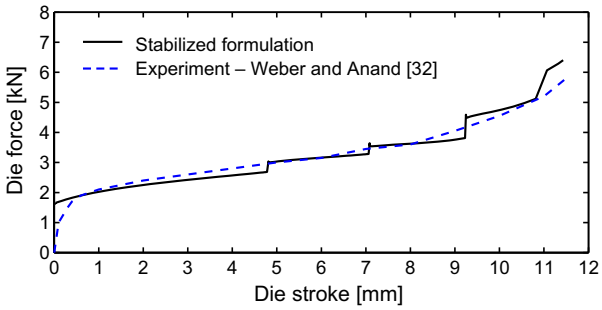

Fig. 22. Die force vs displacement for axisymmetric upsetting of 1100 Al.

come in contact with the die. Making the mesh fine in these regions will reduce the magnitude of these jumps.

7. Conclusions

An updated Lagrangian stabilized finite element method, where mesh dependent terms are added element-wise to the usual mixed method, is presented for elastic–plastic finite deformations. Numerical examples are performed using linear stabilized elements with different constitutive laws to demonstrate the advantage of the stabilized finite element formulation. It was seen that the solution obtained with linear elements compare favorably with stable elements (satisfying the Babuška–Brezzi condition) and could lead to a reduction in the degrees of freedom (see Table 3) when stable elements have to be chosen due to the incompressible behavior of the material. The effect of the non-dimensional stability parameter was studied and an alternative scaling parameter was proposed for problems involving elastic–plastic deformations.

This parameter can either be used in the denominator of the stabilization coefficient (δ) or to provide insight into a good range from which to select the stabilization parameter (α) for problems involving elastic–plastic deformations. This formulation is being used as the analysis tool to determine optimal forming parameters using a multi-tier optimization algorithm.

Acknowledgment

This work has been supported by the National Science Foundation through the grant DMI-9634920.

Appendix I

Implicit integration of Eq. (13) over an increment from t_n to t_{n+1} yields

$$\boldsymbol{F}^{\mathrm{p}}_{n+1} = \exp(\Delta t \widehat{\boldsymbol{D}}^{\mathrm{p}}_{n+1})\boldsymbol{F}^{\mathrm{p}}_{n}. \tag{45}$$

Integrating evolution Eq. (18) using a backward Euler scheme gives

$$s_{n+1} = s_n + \Delta t g(\dot{\varepsilon}^{\mathrm{p}}_{n+1}, s_{n+1}). \tag{46}$$

Let $\boldsymbol{F}^{\mathrm{e}}_{*} = \boldsymbol{F}_{n+1}\boldsymbol{F}^{\mathrm{p}-1}_{n}$ be the trial elastic deformation gradient. Performing the polar decomposition of $\boldsymbol{F}^{\mathrm{e}}_{*}$ and $\boldsymbol{F}^{\mathrm{e}}_{n+1}$ and using Eq. (45) we can write

$$\boldsymbol{F}^{\mathrm{e}}_{*} = \boldsymbol{R}^{\mathrm{e}}_{*}\boldsymbol{U}^{\mathrm{e}}_{*} = \boldsymbol{F}^{\mathrm{e}}_{n+1}\boldsymbol{F}^{\mathrm{p}}_{n+1}\boldsymbol{F}^{\mathrm{p}-1}_{n} = \boldsymbol{R}^{\mathrm{e}}_{n+1}\boldsymbol{U}^{\mathrm{e}}_{n+1}\exp(\Delta t \widehat{\boldsymbol{D}}^{\mathrm{p}}_{n+1}). \tag{47}$$

From Eqs. (7), (8), (10), (14) and (15) it can be shown that $\boldsymbol{U}^{\mathrm{e}}_{n+1}$ and $\exp(\Delta t \widehat{\boldsymbol{D}}^{\mathrm{p}}_{n+1})$ have the same eigenvectors, i.e. they commute, due to the isotropic nature of the constitutive laws (8) and (14). Therefore $\boldsymbol{U}^{\mathrm{e}}_{n+1}\exp(\Delta t \widehat{\boldsymbol{D}}^{\mathrm{p}}_{n+1})$ is symmetric. Then by uniqueness of the polar decomposition

$$\boldsymbol{R}^{\mathrm{e}}_{*} = \boldsymbol{R}^{\mathrm{e}}_{n+1}, \tag{48}$$

$$\boldsymbol{U}^{\mathrm{e}}_{*} = \boldsymbol{U}^{\mathrm{e}}_{n+1}\exp(\Delta t \widehat{\boldsymbol{D}}^{\mathrm{p}}_{n+1}). \tag{49}$$

Taking the logarithm of Eq. (49)

$$\widehat{\boldsymbol{E}}^{\mathrm{e}}_{*} = \widehat{\boldsymbol{E}}^{\mathrm{e}}_{n+1} + \Delta t \widehat{\boldsymbol{D}}^{\mathrm{p}}_{n+1}, \tag{50}$$

where $\widehat{\boldsymbol{E}}^{\mathrm{e}}_{*} = \ln \boldsymbol{U}^{\mathrm{e}}_{*}$. Applying the the elasticity operator (8) to Eq. (50) and using Eqs. (7) and (14), we obtain

$$\widehat{\boldsymbol{T}}_{*} = \widehat{\boldsymbol{T}}_{n+1} + \sqrt{6}\mu\Delta t\dot{\varepsilon}^{\mathrm{p}}_{n+1}\widehat{\boldsymbol{N}}_{n+1}. \tag{51}$$

Taking the deviatoric component and using (15)

$$\widehat{\boldsymbol{T}}'_{*} = \sqrt{\frac{2}{3}}\sigma_{n+1}\widehat{\boldsymbol{N}}_{n+1} + \sqrt{6}\mu\Delta t\dot{\varepsilon}^{\mathrm{p}}_{n+1}\widehat{\boldsymbol{N}}_{n+1} \qquad \sqrt{\frac{2}{3}}\sigma_{*}\widehat{\boldsymbol{N}}_{*} = \left(\sqrt{\frac{2}{3}}\sigma_{n+1} + \sqrt{6}\mu\Delta t\dot{\varepsilon}^{\mathrm{p}}_{n+1}\right)\widehat{\boldsymbol{N}}_{n+1}. \tag{52}$$

Therefore

$$\sigma_{*} = \sigma_{n+1} + 3\mu\Delta t\dot{\varepsilon}^{\mathrm{p}}_{n+1} \tag{53}$$

and

$$\widehat{\boldsymbol{N}}_{n+1} = \widehat{\boldsymbol{N}}_{*}. \tag{54}$$

Eqs. (53) and (46) using the constitutive function (17)

$$\begin{aligned} &\sigma_{n+1} - \sigma_* + 3\mu\Delta t f(\sigma_{n+1}, s_{n+1}) = 0, \\ &s_{n+1} - s_n - \Delta t g(f(\sigma_{n+1}, s_{n+1}), s_{n+1}) = 0 \end{aligned} \tag{55}$$

are solved simultaneously for σ_{n+1} and s_{n+1}.

The integration algorithm proceeds as follows:

(1) Compute the deformation gradient at t_{n+1}

$$\boldsymbol{F}_{n+1} = \boldsymbol{F}_r \boldsymbol{F}_n. \tag{56}$$

(2) Compute trial elastic deformation gradient

$$\boldsymbol{F}^{\mathrm{e}}_* = \boldsymbol{F}_{n+1} \boldsymbol{F}^{\mathrm{p}-1}_n. \tag{57}$$

(3) Perform the right polar decomposition

$$\boldsymbol{F}^{\mathrm{e}}_* = \boldsymbol{R}^{\mathrm{e}}_* \boldsymbol{U}^{\mathrm{e}}_*. \tag{58}$$

(4) Compute trial elastic logarithmic strain using the spectral decomposition

$$\widehat{\boldsymbol{E}}^{\mathrm{e}}_* = \ln \boldsymbol{U}^{\mathrm{e}}_* = \sum_{\alpha=1}^{3} \ln(\lambda^*_\alpha) \boldsymbol{n}_\alpha \otimes \boldsymbol{n}_\alpha, \tag{59}$$

where λ^*_α and $\boldsymbol{n}_\alpha$ are the eigenvalues and eigenvectors of $\boldsymbol{U}^{\mathrm{e}}_*$.

(5) Compute trial stress

$$\widehat{\boldsymbol{T}}_* = 2\mu \widehat{\boldsymbol{E}}^{\mathrm{e}}_* + \left(\kappa - \frac{2}{3}\mu\right)(\operatorname{tr} \widehat{\boldsymbol{E}}^{\mathrm{e}}_*)\boldsymbol{I}. \tag{60}$$

(6) Compute trial pressure

$$p_* = \tfrac{1}{3}\operatorname{tr}(\widehat{\boldsymbol{T}}_*). \tag{61}$$

(7) Compute deviatoric trial stress

$$\widehat{\boldsymbol{T}}'_* = \widehat{\boldsymbol{T}}_* - p_* \boldsymbol{I}. \tag{62}$$

(8) Compute effective trial stress

$$\sigma_* = \sqrt{\frac{3}{2} \widehat{\boldsymbol{T}}'_* \cdot \widehat{\boldsymbol{T}}'_*}. \tag{63}$$

(9) Solve nonlinear system of equations for σ_{n+1} and s_{n+1}

$$\begin{aligned} &\sigma_{n+1} - \sigma_* + 3\mu\Delta t f(\sigma_{n+1}, s_{n+1}) = 0, \\ &s_{n+1} - s_n - \Delta t g(f(\sigma_{n+1}, s_{n+1}), s_{n+1}) = 0. \end{aligned} \tag{64}$$

(10) Update the stress $\widehat{\boldsymbol{T}}$ with $\hat{p}_{n+1}$ obtained from the finite element update (see Sections 4 and 5)

$$\widehat{\boldsymbol{T}}_{n+1} = \widehat{\boldsymbol{T}}'_{n+1} + \hat{p}_{n+1}\boldsymbol{I} = \eta_{n+1} \widehat{\boldsymbol{T}}'_* + \hat{p}_{n+1}\boldsymbol{I} \quad \text{where } \eta_{n+1} = \frac{\sigma_{n+1}}{\sigma_*}. \tag{65}$$

(11) Transform $\widehat{\boldsymbol{T}}$ to $\boldsymbol{T}$ (the Cauchy stress on B_{n+1})

$$\boldsymbol{T}_{n+1} = \frac{1}{\det \boldsymbol{F}_{n+1}} \boldsymbol{R}^{\mathrm{e}}_* \widehat{\boldsymbol{T}}_{n+1} \boldsymbol{R}^{\mathrm{e}\,\mathrm{T}}_* \tag{66}$$

(12) Compute $\widehat{\boldsymbol{D}}^{\mathrm{p}}_{n+1}$

$$\widehat{\boldsymbol{D}}^{\mathrm{p}}_{n+1} = \sqrt{\frac{3}{2}}\dot{\bar{\varepsilon}}^{\mathrm{p}}_{n+1}\widehat{\boldsymbol{N}}_{n+1} \tag{67}$$

where $\dot{\bar{\varepsilon}}^{\mathrm{p}}_{n+1} = f(\sigma_{n+1}, s_{n+1})$ and $\widehat{\boldsymbol{N}}_{n+1} = \widehat{\boldsymbol{N}}_{*} = \sqrt{\frac{3}{2}}\frac{\widehat{\boldsymbol{T}}'_{*}}{\sigma_{*}}$.

(13) Compute $\boldsymbol{F}^{\mathrm{p}}_{n+1}$

$$\begin{aligned} &\boldsymbol{F}^{\mathrm{p}}_{n+1} = \exp(\Delta t\widehat{\boldsymbol{D}}^{\mathrm{p}}_{n+1})\boldsymbol{F}^{\mathrm{p}}_{n} \\ &\exp(\Delta t\widehat{\boldsymbol{D}}^{\mathrm{p}}_{n+1}) = \sum\nolimits_{\alpha=1}^{3}\exp(\Delta t d^{\mathrm{p}}_{\alpha})\boldsymbol{n}_{\alpha}\otimes\boldsymbol{n}_{\alpha} \end{aligned} \tag{68}$$

where d^{p}_{α} and $\boldsymbol{n}_{\alpha}$ are the eigenvalues and eigenvectors of $\widehat{\boldsymbol{D}}^{\mathrm{p}}_{n+1}$.

(14) Compute elastic part of the deformation gradient $\boldsymbol{F}^{\mathrm{e}}_{n+1}$

$$\boldsymbol{F}^{\mathrm{e}}_{n+1} = \boldsymbol{F}_{n+1}\boldsymbol{F}^{\mathrm{p}-1}_{n+1}. \tag{69}$$

The algorithm for rate independent plasticity is similar to the one presented above. For details, refer to the papers by Weber et al. [32] and Eterovic and Bathe [6].

Appendix II

The linearization of the first Piola–Kirchoff stress $\boldsymbol{P}_r$, required in Eq. (31), using Eq. $(21)_1$ and $\frac{\det \boldsymbol{F}_r}{\det \boldsymbol{F}_{n+1}} = \frac{1}{\det \boldsymbol{F}_n}$ yields

$$\begin{aligned} D_{\boldsymbol{u}}[\boldsymbol{P}_r(\boldsymbol{u},p)]\Delta\boldsymbol{u} = \frac{1}{(\det \boldsymbol{F}_n)}\Big\{ &(D_{\boldsymbol{u}}[\boldsymbol{R}^{\mathrm{e}}_{*}]\Delta\boldsymbol{u})\,\widehat{\boldsymbol{T}}'_{n+1}\boldsymbol{R}^{\mathrm{e}\mathrm{T}}_{*}\boldsymbol{F}^{-\mathrm{T}}_{r} + \boldsymbol{R}^{\mathrm{e}}_{*}\widehat{\boldsymbol{T}}'_{n+1}(D_{\boldsymbol{u}}[\boldsymbol{R}^{\mathrm{e}\mathrm{T}}_{*}]\Delta\boldsymbol{u})\boldsymbol{F}^{-\mathrm{T}}_{r} \\ &+ \boldsymbol{R}^{\mathrm{e}}_{*}(D_{\boldsymbol{u}}[\widehat{\boldsymbol{T}}'_{n+1}]\Delta\boldsymbol{u})\boldsymbol{R}^{\mathrm{e}}_{*}\boldsymbol{F}^{-\mathrm{T}}_{r} - \boldsymbol{R}^{\mathrm{e}}_{*}\widehat{\boldsymbol{T}}'_{n+1}\boldsymbol{R}^{\mathrm{e}\mathrm{T}}_{*}\boldsymbol{F}^{-\mathrm{T}}_{r}[\nabla(\Delta\boldsymbol{u})]^{\mathrm{T}}\boldsymbol{F}^{-\mathrm{T}}_{r} - (p_n+p)\boldsymbol{F}^{-\mathrm{T}}_{r}[\nabla(\Delta\boldsymbol{u})]^{\mathrm{T}}\boldsymbol{F}^{-\mathrm{T}}_{r}\Big\}. \end{aligned} \tag{70}$$

Using deviatoric part of Eq. (66)

$$\widehat{\boldsymbol{T}}'_{n+1} = (\det \boldsymbol{F}_{n+1})\boldsymbol{R}^{\mathrm{e}\mathrm{T}}_{*}\boldsymbol{T}'_{n+1}\boldsymbol{R}^{\mathrm{e}}_{*},$$

$D_{\boldsymbol{u}}[\boldsymbol{P}_r(\boldsymbol{u},p)]\Delta\boldsymbol{u}$ can be written as

$$\begin{aligned} D_{\boldsymbol{u}}[\boldsymbol{P}_r(\boldsymbol{u},p)]\Delta\boldsymbol{u} = &(\det \boldsymbol{F}_r)(D_{\boldsymbol{u}}[\boldsymbol{R}^{\mathrm{e}}_{*}]\Delta\boldsymbol{u})\boldsymbol{R}^{\mathrm{e}\mathrm{T}}_{*}\boldsymbol{T}'_{n+1}\boldsymbol{F}^{-\mathrm{T}}_{r} + (\det \boldsymbol{F}_r)\boldsymbol{T}'_{n+1}\boldsymbol{R}^{\mathrm{e}}_{*}(D_{\boldsymbol{u}}[\boldsymbol{R}^{\mathrm{e}\mathrm{T}}_{*}]\Delta\boldsymbol{u})\boldsymbol{F}^{-\mathrm{T}}_{r} \\ &+ \frac{1}{(\det \boldsymbol{F}_n)}\boldsymbol{R}^{\mathrm{e}}_{*}(D_{\boldsymbol{u}}[\widehat{\boldsymbol{T}}'_{n+1}]\Delta\boldsymbol{u})\boldsymbol{R}^{\mathrm{e}}_{*}\boldsymbol{F}^{-\mathrm{T}}_{r} - (\det \boldsymbol{F}_r)\boldsymbol{T}_{n+1}\boldsymbol{F}^{-\mathrm{T}}_{r}[\nabla(\Delta\boldsymbol{u})]^{\mathrm{T}}\boldsymbol{F}^{-\mathrm{T}}_{r}, \end{aligned} \tag{71}$$

where

$$D_{\boldsymbol{u}}[\widehat{\boldsymbol{T}}'_{n+1}]\Delta\boldsymbol{u} = \widehat{\mathscr{L}}' : D_{\boldsymbol{u}}[\widehat{\boldsymbol{E}}^{\mathrm{e}}_{*}]\Delta\boldsymbol{u}. \tag{72}$$

In the case of a viscoplastic material with flow function $\dot{\bar{\varepsilon}}^{\mathrm{p}} = f(\sigma, s)$ and evolution equation for the state variable $\dot{s} = \tilde{g}(\sigma, s) = g(f(\sigma, s), s)$, the material stiffness $\widehat{\mathscr{L}}'$ is given by [32]

$$\widehat{\mathscr{L}}' = 2\mu\left(1 - 3\mu\Delta t\frac{\dot{\bar{\varepsilon}}^{\mathrm{p}}}{\sigma_{*}}\right)\left(\boldsymbol{\Pi} - \frac{1}{3}\boldsymbol{I}\otimes\boldsymbol{I}\right) + 2\mu\left(3\mu\Delta t\frac{\dot{\bar{\varepsilon}}^{\mathrm{p}}}{\sigma_{*}} - 1 + c\right)\widehat{\boldsymbol{N}}\otimes\widehat{\boldsymbol{N}}, \tag{73}$$

where

$$c = \frac{b_2}{a_1 b_2 + a_2 b_1}, \tag{74}$$

$$a_1 = 1 + 3\mu\Delta t \frac{\partial f}{\partial \sigma},$$

$$a_2 = 3\mu\Delta t \frac{\partial f}{\partial s},$$

$$b_1 = \Delta t \frac{\partial \tilde{g}}{\partial \sigma},$$

$$b_2 = 1 - \Delta t \frac{\partial \tilde{g}}{\partial s}.$$

For rate independent plasticity the consistent elasto-plastic stiffness $\widehat{\mathscr{L}}'$ is given by [31]

$$\widehat{\mathscr{L}}' = 2\mu\left(1 - 3\mu\frac{\Delta\varepsilon^{\mathrm{p}}}{\sigma_*}\right)\left(\boldsymbol{\Pi} - \frac{1}{3}\boldsymbol{I}\otimes\boldsymbol{I}\right) + 2\mu\left(3\mu\frac{\Delta\varepsilon^{\mathrm{p}}}{\sigma_*} - \frac{1}{1+\frac{H}{3\mu}}\right)\widehat{\boldsymbol{N}}\otimes\widehat{\boldsymbol{N}}. \tag{75}$$

The derivatives of the trial rotation and right stretch tensors $\boldsymbol{R}^{\mathrm{e}}_*$ and $\boldsymbol{U}^{\mathrm{e}}_*$ required in Eq. (71) can be found using the results obtained in Chen and Wheeler [4] and Rosati [24]

$$D_{\boldsymbol{u}}[\boldsymbol{R}^{\mathrm{e}}_*]\Delta\boldsymbol{u} = \frac{1}{\det \boldsymbol{Y}^{\mathrm{e}}_*}\boldsymbol{R}^{\mathrm{e}}_*\boldsymbol{Y}^{\mathrm{e}}_*\left\{\boldsymbol{R}^{\mathrm{e}\,\mathrm{T}}_*(D_{\boldsymbol{u}}[\boldsymbol{F}^{\mathrm{e}}_*]\Delta\boldsymbol{u}) - (D_{\boldsymbol{u}}[\boldsymbol{F}^{\mathrm{e}}_*]\Delta\boldsymbol{u})^{\mathrm{T}}\boldsymbol{R}^{\mathrm{e}}_*\right\}\boldsymbol{Y}^{\mathrm{e}}_*, \tag{76}$$

$$D_{\boldsymbol{u}}[\boldsymbol{U}^{\mathrm{e}}_*]\Delta\boldsymbol{u} = \boldsymbol{R}^{\mathrm{e}\,\mathrm{T}}_*(D_{\boldsymbol{u}}[\boldsymbol{F}^{\mathrm{e}}_*]\Delta\boldsymbol{u}) - \frac{1}{\det \boldsymbol{Y}^{\mathrm{e}}_*}\boldsymbol{Y}^{\mathrm{e}}_*\left\{\boldsymbol{R}^{\mathrm{e}\,\mathrm{T}}_*(D_{\boldsymbol{u}}[\boldsymbol{F}^{\mathrm{e}}_*]\Delta\boldsymbol{u}) - (D_{\boldsymbol{u}}[\boldsymbol{F}^{\mathrm{e}}_*]\Delta\boldsymbol{u})^{\mathrm{T}}\boldsymbol{R}^{\mathrm{e}}_*\right\}\boldsymbol{Y}^{\mathrm{e}}_*\boldsymbol{U}^{\mathrm{e}}_*, \tag{77}$$

where

$$\boldsymbol{Y}^{\mathrm{e}}_* = \mathrm{tr}(\boldsymbol{U}^{\mathrm{e}}_*)\boldsymbol{I} - \boldsymbol{U}^{\mathrm{e}}_*$$

and

$$D_{\boldsymbol{u}}[\boldsymbol{F}^{\mathrm{e}}_*]\Delta\boldsymbol{u} = \nabla(\Delta\boldsymbol{u})\boldsymbol{F}^{\mathrm{e}}_n. \tag{78}$$

The linearization of $\widehat{\boldsymbol{E}}^{\mathrm{e}}_*$ is done following the work of Hogar [9]. When the eigenvalues of $\boldsymbol{U}^{\mathrm{e}}_*$ (λ_1, λ_2 and λ_3) are unique i.e. $\lambda_1 \neq \lambda_2 \neq \lambda_3 \neq \lambda_1$ the linearization gives

$$\begin{aligned}
D_{\boldsymbol{u}}[\widehat{\boldsymbol{E}}^{\mathrm{e}}_*]\Delta\boldsymbol{u} = {} & (\mathscr{F}_1 + \mathscr{F}_2 + \mathscr{F}_3)\boldsymbol{C}^{\mathrm{e}}_*(D_{\boldsymbol{u}}[\boldsymbol{U}^{\mathrm{e}}_*]\Delta\boldsymbol{u})\boldsymbol{C}^{\mathrm{e}}_* \\
& - [(\lambda_1+\lambda_2)\mathscr{F}_3 + (\lambda_2+\lambda_3)\mathscr{F}_1 + (\lambda_3+\lambda_1)\mathscr{F}_2]\left\{\boldsymbol{C}^{\mathrm{e}}_*(D_{\boldsymbol{u}}[\boldsymbol{U}^{\mathrm{e}}_*]\Delta\boldsymbol{u})\boldsymbol{U}^{\mathrm{e}}_* + \boldsymbol{U}^{\mathrm{e}}_*(D_{\boldsymbol{u}}[\boldsymbol{U}^{\mathrm{e}}_*]\Delta\boldsymbol{u})\boldsymbol{C}^{\mathrm{e}}_*\right\} \\
& + (\lambda_1\lambda_2\mathscr{F}_3 + \lambda_2\lambda_3\mathscr{F}_1 + \lambda_3\lambda_1\mathscr{F}_2)\left\{\boldsymbol{C}^{\mathrm{e}}_*(D_{\boldsymbol{u}}[\boldsymbol{U}^{\mathrm{e}}_*]\Delta\boldsymbol{u}) + (D_{\boldsymbol{u}}[\boldsymbol{U}^{\mathrm{e}}_*]\Delta\boldsymbol{u})\boldsymbol{C}^{\mathrm{e}}_*\right\} \\
& + [(\lambda_1+\lambda_2)^2\mathscr{F}_3 + (\lambda_2+\lambda_3)^2\mathscr{F}_1 + (\lambda_3+\lambda_1)^2\mathscr{F}_2]\boldsymbol{U}^{\mathrm{e}}_*(D_{\boldsymbol{u}}[\boldsymbol{U}^{\mathrm{e}}_*]\Delta\boldsymbol{u})\boldsymbol{U}^{\mathrm{e}}_* \\
& + [-\lambda_1\lambda_2(\lambda_1+\lambda_2)\mathscr{F}_3 - \lambda_2\lambda_3(\lambda_2+\lambda_3)\mathscr{F}_1 - \lambda_3\lambda_1(\lambda_3+\lambda_1)\mathscr{F}_2 + (\mathscr{G}_1+\mathscr{G}_2+\mathscr{G}_3)] \\
& \times \left\{\boldsymbol{U}^{\mathrm{e}}_*(D_{\boldsymbol{u}}[\boldsymbol{U}^{\mathrm{e}}_*]\Delta\boldsymbol{u}) + (D_{\boldsymbol{u}}[\boldsymbol{U}^{\mathrm{e}}_*]\Delta\boldsymbol{u})\boldsymbol{U}^{\mathrm{e}}_*\right\} \\
& + [(\lambda_1\lambda_2)^2\mathscr{F}_3 + (\lambda_2\lambda_3)^2\mathscr{F}_1 + (\lambda_3\lambda_1)^2\mathscr{F}_2 - (\lambda_1+\lambda_2)\mathscr{G}_3 - (\lambda_2+\lambda_3)\mathscr{G}_1 - (\lambda_3+\lambda_1)\mathscr{G}_2] \\
& \times (D_{\boldsymbol{u}}[\boldsymbol{U}^{\mathrm{e}}_*]\Delta\boldsymbol{u}),
\end{aligned} \tag{79}$$

when $\lambda_i \neq \lambda_j = \lambda_k \equiv \lambda$ the linearization is

$$D_{\boldsymbol{u}}[\widehat{\boldsymbol{E}}^{\mathrm{e}}_*]\Delta\boldsymbol{u} = \frac{1}{(\lambda_i-\lambda)^3}\left[\left\{(\lambda_i-\lambda)\left(\frac{1}{\lambda_i}+\frac{1}{\lambda}\right) - 2\ln\left(\frac{\lambda_i}{\lambda}\right)\right\}\boldsymbol{U}^{\mathrm{e}}_*(D_{\boldsymbol{u}}[\boldsymbol{U}^{\mathrm{e}}_*]\Delta\boldsymbol{u})\boldsymbol{U}^{\mathrm{e}}_* + \left\{-(\lambda_i-\lambda)\left(\frac{\lambda}{\lambda_i}+\frac{\lambda_i}{\lambda}\right) + (\lambda_i+\lambda)\ln\left(\frac{\lambda_i}{\lambda}\right)\right\}\left\{\boldsymbol{U}^{\mathrm{e}}_*(D_{\boldsymbol{u}}[\boldsymbol{U}^{\mathrm{e}}_*]\Delta\boldsymbol{u}) + (D_{\boldsymbol{u}}[\boldsymbol{U}^{\mathrm{e}}_*]\Delta\boldsymbol{u})\boldsymbol{U}^{\mathrm{e}}_*\right\} + \left\{(\lambda_i-\lambda)\left(\frac{\lambda^2}{\lambda_i}+\frac{\lambda_i^2}{\lambda}\right) - 2\lambda_i\lambda\ln\left(\frac{\lambda_i}{\lambda}\right)\right\}(D_{\boldsymbol{u}}[\boldsymbol{U}^{\mathrm{e}}_*]\Delta\boldsymbol{u})\right] \tag{80}$$

and $\lambda_1 = \lambda_2 = \lambda_3 \equiv \lambda$ gives

$$D_{\boldsymbol{u}}[\widehat{\boldsymbol{E}}^{\mathrm{e}}_*]\Delta\boldsymbol{u} = \frac{1}{\lambda}(D_{\boldsymbol{u}}[\boldsymbol{U}^{\mathrm{e}}_*]\Delta\boldsymbol{u}) \tag{81}$$

where $\boldsymbol{C}^{\mathrm{e}}_* = \boldsymbol{U}^{\mathrm{e}2}_*$ and

$$\mathscr{G}_i = \frac{\ln(\lambda_i)}{(\lambda_i-\lambda_j)(\lambda_i-\lambda_k)},$$

$$\mathscr{F}_i = \frac{1}{(\lambda_i-\lambda_j)^2(\lambda_i-\lambda_k)^2}\left[\frac{1}{\lambda_i} - (\lambda_i-\lambda_j)(\mathscr{G}_{\mathrm{i}}+\mathscr{G}_k) - (\lambda_i-\lambda_k)(\mathscr{G}_{\mathrm{i}}+\mathscr{G}_j)\right].$$

i, j, k being a permutation of 1, 2, 3.

References

[1] F. Brezzi, M. Fortin, Mixed and Hybrid Finite Element Methods, Springer, New York, 1991.
[2] U. Brink, E. Stein, Some mixed finite element methods for incompressible and nearly incompressible elasticity, Computat. Mech. 19 (1996) 105–119.
[3] S.B. Brown, K.H. Kim, L. Anand, An internal variable constitutive model for the hot working of metals, Int. J. Plast. 5 (1989) 95–130.
[4] Y.C. Chen, L. Wheeler, Derivatives of the stretch and rotation tensors, J. Elast. 32 (1993) 175–182.
[5] M. Chiumenti, Q. Valverde, C. Agelet de Saracibar, M. Cervera, A stabilized formulation for incompressible elasticity using linear displacement and pressure interpolations, Comput. Methods Appl. Mech. Engrg. 191 (2002) 5253–5264.
[6] A.L. Eterovic, K.J. Bathe, A Hyperelastic-based large strain elasto-plastic constitutive formulation with combined isotropic-kinematic hardening using the logarithmic stress and strain measures, Int. J. Numer. Meth. Engrg. 30 (1990) 1099–1114.
[7] L.P. Franca, T.J.R. Hughes, R. Stenberg, Stabilized finite element methods, in: M. Gunzburger, R.A. Nicolaides (Eds.), Incompressible Computational Fluid Dynamics, Cambridge University Press, 1993, pp. 87–107, (Chapter 4).
[8] H.D. Hibbitt, P.V. Marcal, J.R. Rice, A finite element formulation for problems of large strain and large displacement, Int. J. Solids Struct. 6 (1970) 1069–1086.
[9] A. Hogar, The material time derivative of logarithmic strain, Int. J. Solids Struct. 22 (1986) 1019–1032.
[10] A. Hogar, The stress conjugate to logarithmic strain, Int. J. Solids Struct. 23 (1987) 1645–1656.
[11] T.J.R. Hughes, L.P. Franca, M. Balestra, A new finite element formulation for computational fluid dynamics: V. Circumventing the Babuška–Brezzi condition: a stable Petrov–Galerkin formulation of the stokes problem accommodating equal-order interpolations, Comput. Methods Appl. Mech. Engrg. 59 (1985) 85–99.
[12] T.J.R. Hughes, L.P. Franca, A new finite element formulation for computational fluid dynamics: VII. The stokes problem with various well-posed boundary conditions: symmetric formulations that converge for all velocity/pressure spaces, Comput. Methods Appl. Mech. Engrg. 65 (1987) 85–96.
[13] T.J.R. Hughes, Multiscale phenomena: Green's function, Dirichlet-to-formulation, subgrid formulation, subgrid scale models, bubbles and the origins of stabilized methods, Comput. Methods Appl. Mech. Engrg. 127 (1995) 387–401.
[14] O. Klaas, A.M. Maniatty, M.S. Shephard, A stabilized mixed finite element method for finite elasticity: formulation for linear displacement and pressure interpolation, Comput. Methods Appl. Mech. Engrg. 180 (1999) 65–79.
[15] E.H. Lee, Elastic–plastic deformation at finite strain, J. Appl. Mech. 36 (1969) 2–6.
[16] A.M. Lush, G. Weber, L. Anand, An implicit time-integration procedure for a set of internal variable constitutive equations for isotropic elasto-viscoplasticity, Int. J. Plast. 5 (1989) 521–549.

[17] A.M. Maniatty, Y. Liu, O. Klaas, M.S. Shephard, Stabilized finite element method for viscoplastic flow: formulation and a simple progressive solution strategy, Comput. Methods Appl. Mech. Engrg. 190 (2001) 4609–4625.
[18] A.M. Maniatty, Y. Liu, O. Klaas, M.S. Shephard, Higher order stabilized finite element method for hyperelastic finite deformation, Comput. Methods Appl. Mech. Engrg. 191 (2002) 1491–1503.
[19] A.M. Maniatty, Y. Liu, Stabilized finite element method for viscoplastic flow: formulation with state variable evolution, Int. J. Numer. Meth. Engrg. 56 (2003) 185–209.
[20] R.M. McMeeking, J.R. Rice, Finite element formulations for problems of large elastic–plastic deformation, Int. J. Solids Struct. 11 (1975) 601–616.
[21] C. Miehe, E. Stein, W. Wagner, Associative multiplicative elasto-plasticity: Formulation and aspects of the numerical implementation including stability analysis, Comput. Struct. 51 (1994) 969–978.
[22] A. Needleman, A numerical study of necking in circular cylindrical bars, J. Mech. Phys. Solids 20 (1972) 964–970.
[23] B. Moran, M. Ortiz, C.F. Shih, Formulation of implicit finite element methods for multiplicative finite deformation plasticity, Int. J. Numer. Meth. Engrg. 29 (1990) 483–514.
[24] L. Rosati, Derivatives and rates of the stretch and rotation tensors, J. Elast. 56 (1999) 213–230.
[25] D. Rypl, Sequential and parallel generation of unstructured 3D meshes, CTU Rep, 1998 2(3).
[26] J.C. Simo, R.L. Taylor, K.S. Pister, Variational and projection methods for the volume constraint in finite deformation elasto-plasticity, Comput. Methods Appl. Mech. Engrg. 51 (1985) 177–208.
[27] J.C. Simo, M. Ortiz, A unified approach to finite deformation elastoplastic analysis bsed on the use of hyperelastic constitutive equations, Comput. Methods Appl. Mech. Engrg. 49 (1985) 221–245.
[28] J.C. Simo, A framework for finite elastoplasticity based on maximum plastic dissipation and the multiplicative decomposition: Part I. Continuum formulation, Comput. Methods Appl. Mech. Engrg. 66 (1988) 199–219.
[29] J.C. Simo, A framework for finite elastoplasticity based on maximum plastic dissipation and the multiplicative decomposition: Part II. Computational aspects, Comput. Methods Appl. Mech. Engrg. 68 (1988) 1–31.
[30] J.C. Simo, T.A. Laursen, An augmented Lagrangian treatment of contact problems involving friction, Comput. Struct. 42 (1992) 97–116.
[31] J.C. Simo, T.J.R. Hughes, Computational Inelasticity, Springer, New York, 1998.
[32] G. Weber, L. Anand, Finite deformation constitutive equations and a time integration procedure for isotropic, hyperelastsolids solids, Comput. Methods Appl. Mech. Engrg. 79 (1990) 173–202.
[33] P. Wriggers, Finite element algorithms for contact problems, Arch. Computat. Methods Engrg., State-of-the-art Rev. 2 (1995) 1–49.
[34] H. Xiao, O.T. Bruhns, A. Meyers, Logarithmic strain, logarithmic spin and logarithmic rate, Acta Mech. 124 (1997) 89–105.